Interpolating the isotopic composition of modern meteoric precipitation

Gabriel J. Bowen and Justin Revenaugh[1]

Earth Science Department, University of California, Santa Cruz, California, USA

Received 21 February 2003; revised 2 June 2003; accepted 7 August 2003; published 28 October 2003.

[1] An accurate representation of the spatial distribution of stable hydrogen and oxygen isotopes in modern precipitation is required for many hydrological, paleoclimate, and ecological applications. No standardized method for achieving such a representation exists, and potential errors associated with previously employed methods are not understood. Using resampling, we test the accuracy of interpolated δD and $\delta^{18}O$ estimates made using four methods. Prediction error for all methods is strongly related to number of data and will likely decline with the addition of new data. The best method lowers estimation error by 10–15% relative to others tested and gives an average error, using all available data, ≈2.5% of the global range. We present and interpret global maps of interpolated δD, $\delta^{18}O$, and deuterium excess in precipitation and the 95% confidence intervals for these values created using the optimal method. These depict global and regional patterns, make evident the robustness of interpolated isotopic patterns, and highlight target areas for future precipitation sampling. *INDEX TERMS:* 0330 Atmospheric Composition and Structure: Geochemical cycles; 1040 Geochemistry: Isotopic composition/chemistry; 1655 Global Change: Water cycles (1836); *KEYWORDS:* oxygen, deuterium, hydrogen, stable isotopes, meteoric water, maps

Citation: Bowen, G. J., and J. Revenaugh, Interpolating the isotopic composition of modern meteoric precipitation, *Water Resour. Res.*, *39*(10), 1299, doi:10.1029/2003WR002086, 2003.

1. Introduction

[2] The stable oxygen and hydrogen isotope composition of precipitation exhibits spatial variation across Earth's surface. Atmospheric moisture is derived primarily from low-latitude oceanic regions, where its initial composition is fixed by isotope effects related to evaporation and boundary layer diffusion between the ocean and atmosphere [e.g., *Boyle*, 1997]. The δD or $\delta^{18}O$ of precipitation is high in regions where vapor is sourced to the atmosphere, and declines away from source regions in response to the progressive cooling of air masses and equilibrium fractionation between vapor and precipitation during rainout [*Dansgaard*, 1964]. Cooling and rainout occur by any of a number of meteorological processes, including meridional transport, transport from oceanic to continental regions, orographic lifting, and convective processes [*Rozanski et al.*, 1993]. Additional modification of vapor isotope values can result from the contribution of evaporated or transpired meteoric water to atmospheric vapor [*Gat et al.*, 1994; *Pierrehumbert*, 1999]. Spatial variability in the δD or $\delta^{18}O$ of precipitation reflects the combination of source-region labeling, rainout effects, and recycling effects that affect air masses bringing vapor to different geographic regions.

[3] Meteoric water isotopic compositions, measured directly or preserved within minerals or plant or animal tissue, are commonly used in studies of continental climate and hydrology. These studies use δD or $\delta^{18}O$ in one of two ways: as a tracer or to monitor a process. Tracer applications rely directly on the isotopic labeling of atmospheric vapor and/or the resultant spatial variation in meteoric water isotopes to discern the source and mixing of surface or groundwaters [e.g., *Lee et al.*, 1999; *Kendall and Coplen*, 2001], to discern animal migration patterns [e.g., *Hobson and Wassenaar*, 1997], or to infer shifts in the source of precipitation delivered to a study site over time [*Amundson et al.*, 1996; *Genty et al.*, 2002; *Jahren and Sternberg*, 2002]. Process applications focus on factors that control water isotope evolution in atmospheric vapor or the fractionation between meteoric water and oxygen-bearing mineral phases. *Dansgaard* [1964] noted the modern spatial relation between local mean annual temperature and the δD and $\delta^{18}O$ of precipitation, and this relation has been applied in the interpretation of isotopic archive records [e.g., *Hays and Grossman*, 1991; *Dansgaard et al.*, 1993]. Recent work has focused on variables other than local temperature that might control the extent of rainout as vapor is delivered to a study site [*Edwards et al.*, 1996; *Boyle*, 1997; *Chamberlain et al.*, 1999; *Chamberlain and Poage*, 2000; *Poage et al.*, 2000; *Hammarlund et al.*, 2002] or modify the isotopic composition of meteoric water [e.g., *Seltzer et al.*, 2000; *Wolfe et al.*, 2001]. The magnitude of $\delta^{18}O$ fractionation during the precipitation of many minerals is temperature-dependant, and, if the $\delta^{18}O$ of environmental water can be estimated, can be used as a proxy for environmental temperature [e.g., *Emiliani*, 1972; *Lauritzen*, 1996].

[4] A common feature of these applications is that they require knowledge of the isotopic composition of modern meteoric precipitation at one or more locations. The type of information required depends on the application, but in many cases it is desirable to know the integrated isotopic

[1]Now at Department of Geology and Geophysics, University of Minnesota, Twin Cities, Minneapolis, Minnesota, USA.

0043-1397/03/2003WR002086

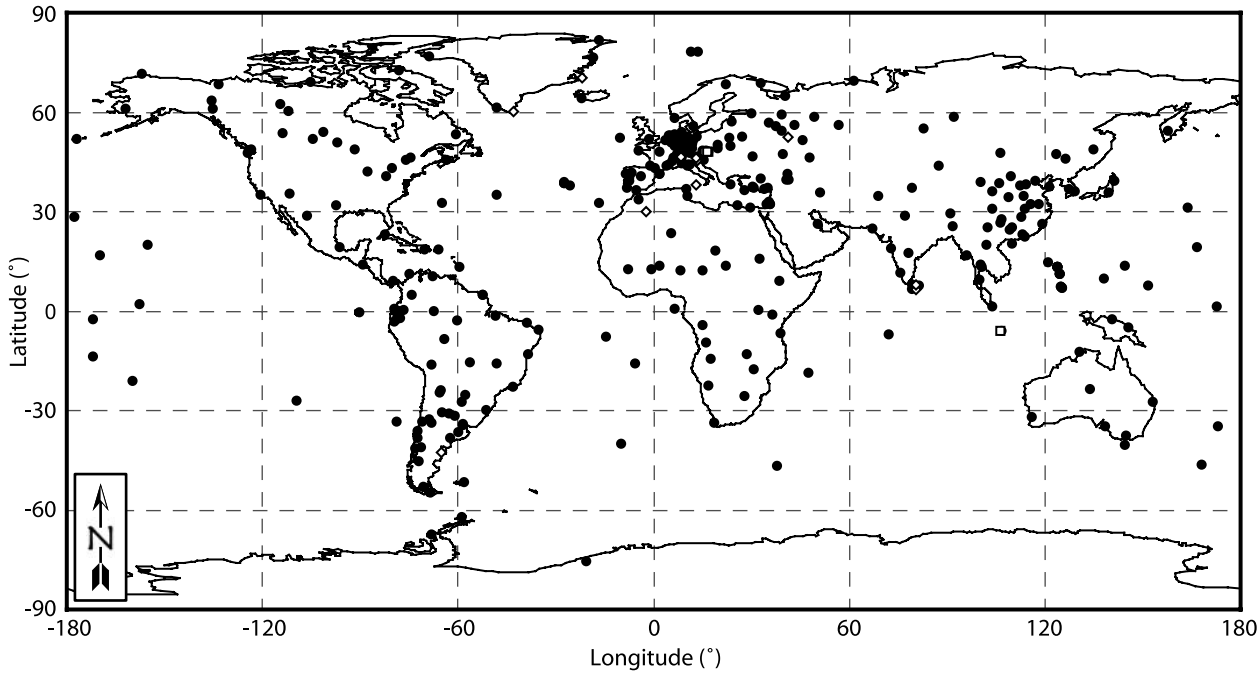

Figure 1. Location of GNIP stations for which mean annual δD or $\delta^{18}O$ data were obtained; δD and $\delta^{18}O$ data are from 336 stations (solid circles), δD only at 4 sites (open squares), and $\delta^{18}O$ only at 12 sites (open diamonds).

composition of modern precipitation delivered in an "average" year (the long-term, mean annual δD or $\delta^{18}O$). In actuality, records of the stable isotope composition of precipitation spanning one or more years are available for only a few hundred locations worldwide (Figure 1). For some specific applications, it is possible to estimate the mean isotopic composition of modern local precipitation through one or more years of direct measurement. Although desirable, direct measurement is time consuming and, for regional or global scale studies, logistically unfeasible. In addition, short-term climatic variation may bias estimates of long-term annual precipitation δD or $\delta^{18}O$ derived from only one or two years of data. Together, these concerns highlight the need for methods that allow the point estimation of δD and $\delta^{18}O$ from existing data sets.

[5] Spatial interpolation provides a method for estimating the isotopic composition of precipitation where data are not available by generating a smoothed trend surface that captures the geographic variability of data. In addition to providing point estimates, examination of the deviation of individual data values from the trend surface can highlight values that are unusual in their geographic context. Also, the representation of discrete data by a continuous trend surface can allow comparison between data of different spatial scale or resolution. For instance, a robust method for the spatial interpolation of δD and $\delta^{18}O$ values of precipitation might improve comparisons between monitoring station measurements and the output of isotope tracer-equipped general circulation models, which operate on a coarse grid resolution [*Jouzel et al.*, 2000; *Mathieu et al.*, 2002].

[6] Most previous work requiring point estimates of the δD or $\delta^{18}O$ of precipitation, or attempting to spatially represent the global water isotopes in precipitation data set, has relied on simple spatial interpolation methods (contouring, triangulation, and inverse distance methods). Recently, two more complex methods for interpolation of the isotopic composition of precipitation have been applied. In the fall of 2001 a group working with the IAEA released a series of maps representing the oxygen and hydrogen isotope composition of precipitation as estimated by Cressman objective analysis [*Birks et al.*, 2002], a spheres of influence interpolation method developed in the 1950s for interpolation of meteoric data [*Cressman*, 1959]. Subsequently, *Bowen and Wilkinson* [2002] developed an interpolation scheme that combines an empirical model for isotopic trends related to latitude and altitude (through the temperature effect) with spatial interpolation. Here we quantitatively compare long-term, mean annual δD and $\delta^{18}O$ predictions made using different interpolation methods. We then develop optimal maps of the spatial distribution of oxygen and hydrogen isotopes in precipitation and provide a spatial representation of the confidence levels of these estimations. Finally, we illustrate the utility of these maps by generating and analyzing a global map of deuterium excess that highlights significant regional D excess anomalies. Along the way we consider several interesting features of the existing water isotopes in precipitation data set.

2. Data

[7] The data on the deuterium and oxygen isotope composition of precipitation used for this study come from the most recent release of the Global Network for Isotopes in Precipitation (GNIP) database (http://isohis.iaea.org, 2001). Although this database contains the most comprehensive, global observation set for water isotopes in precipitation, there are some new, independently generated data that have not yet been incorporated in the GNIP data set or in our analysis [e.g., *Welker*, 2000]. All isotopic compositions are given in per mil (‰) units and δ notation relative to the V-

SMOW standard, where $\delta = (R_{sample} - R_{standard})/R_{standard} \times 1000$, and R indicates the ratio D/H or $^{18}O/^{16}O$. Raw data, reporting the isotopic composition and amount of precipitation averaged monthly, were reduced to precipitation-amount-weighted, mean annual values using the method described by *Bowen and Wilkinson* [2002]. The mean annual δD value of precipitation is available for 340 sites; the $\delta^{18}O$ value is available for 348 locations (Figure 1). The elevations of several stations were not available in this data set and were estimated using the United States Geological Survey's GTOPO30 digital elevation model [*U.S. Geological Survey*, 1996], which provides 30 arc second spatial resolution.

[8] Although the GNIP data set is currently the most complete and best available for determining the spatial distribution of isotopes in modern precipitation, it presents at least two important limitations for this kind of work. First, as is evident in Figure 1, the spatial distribution of sampling sites is widely variable, and there are large areas of some continents (e.g., much of the United States, Africa, and central Asia) for which no data are available. *Bowen and Wilkinson* [2002] showed that although global trends account for much of the variability in the $\delta^{18}O$ of precipitation, additional variability of several per mil is present at regional scales. Currently, all methods for the estimation of δD and $\delta^{18}O$ values of precipitation between sampling sites rely on weighting of nearby data to reveal this regional variability; thus data availability limits the accuracy and resolution of these methods in many areas. Second, the GNIP data set represents a compilation of data collected over almost 40 years, and data for all years is not available for all stations. If our goal is to represent the mean modern state of the hydrologic system, we must allow that some erroneous patterns may arise as the result of the uneven distribution of isotope data over time, and the existence of both short term (interannual) variability and long term (decadal) trends in climate during the last four decades. Each of these factors will be taken into consideration in our analysis.

3. Methods

3.1. Comparison of Interpolation Schemes

[9] We estimated the error of interpolated δD and $\delta^{18}O$ estimates by subsampling the GNIP data set (jackknifing [e.g., *Tichelaar and Ruff*, 1989]) and using the remaining observations to predict the isotopic composition of precipitation at measurement sites that were excluded from the subsampled data set. Jackknifes were performed for multiple subsample sizes $n = N - j$, where N represents the total number of available data and j was assigned values between 1 and $N - 50$. For $j = 1$, N subsamples were created where each site was excluded from one subsample. For higher values of j, we generated a large number of subsamples by excluding j randomly selected data from each subsample. At least 100 subsamples were taken at each value of j and, where necessary, a greater number were taken to allow at least 4,000 estimates of δD or $\delta^{18}O$ at unsampled stations. By bootstrapping the subsample error estimates, we found these criteria to be sufficient to generate a stable approximation of the mean magnitude of interpolation error with a standard deviation of <0.14‰ for δD and <0.02‰ for $\delta^{18}O$.

[10] Four interpolation schemes were evaluated. Triangulation was chosen to represent simple spatial interpolation with reference only to the nearest data stations, as has been common in paleoclimate studies [e.g., *Sharp and Cerling*, 1998]. For this method, isotopic estimates were made using the equation:

$$\hat{\delta}_x = \frac{\sum_{i=1}^{3} \delta_i D_{xi}}{\sum_{i=1}^{3} D_{xi}}, \tag{1}$$

where $\hat{\delta}_x$ is our estimate of the isotopic composition (δD or $\delta^{18}O$) at the location of interest, and δ_i and D_{xi} represent the isotopic composition of precipitation at the ith closest measurement site and the distance between the location of interest and the ith closest measurement site in arc degrees, respectively.

[11] The second method examined was inverse distance weighting, where estimates of the isotopic composition at a given location were made using all available stations according to:

$$\hat{\delta}_x = \frac{\sum_{i=1}^{n} \delta_i e^{(-D_{xi}/\beta_1)}}{\sum_{i=1}^{n} e^{(-D_{xi}/\beta_1)}}, \tag{2}$$

where β_1 (°) determines the relative weight assigned to nearby data. This algorithm is a simple representative of a class of spatial interpolation methods commonly used in the generation of contour maps. For large values of β_1, regional variations in isotope compositions will be smoothed over large geographic regions. As β_1 approaches 0, variability at small spatial scales will be highlighted where data are present, but regions lacking data will take on the global average value of δD or $\delta^{18}O$.

[12] Third, using Cressman objective analysis [*Cressman*, 1959], we interpolated data values onto a global 2.5° latitude × 2.5° longitude grid which was used to estimate the isotopic composition of precipitation at excluded data stations. An initial estimate for δD or $\delta^{18}O$ at each grid node was calculated by equation 2 using $\beta_1 = 1.5°$. Correction factors over a series of radii of influence were then determined in sequence and used to incrementally modify the initial estimate. The radii used were 25, 17.5, 10, 7.5, 5 and 2.5°, roughly corresponding to the grid cell radii used to make maps of the isotopic composition of precipitation [*Birks et al.*, 2002]. Correction factors were determined from all data lying with a given radius of influence, and were calculated according to:

$$C_{x,k} = \frac{\sum_{i} \left(\delta_i - p_{i,k-1}\right) \frac{r_k^2 - D_{xi}^2}{r_k^2 + D_{xi}^2}}{n_k}. \tag{3}$$

In this equation $C_{x,k}$ is the correction applied at node x determined using the kth radius of influence, $p_{i,k-1}$ is the isotope value predicted at data station i by inverse distance interpolation between the four surrounding grid values calculated at the previous step, r_k is the current radius of influence, n_k is the number of stations within the current radius of influence, and the summation is for all stations

within r_k degrees of the location of interest. As per *Birks et al.* [2002], no predictions were made for locations more than 10° distant from the nearest data station.

[13] Finally, we examined the method proposed by *Bowen and Wilkinson* [2002] (hereafter referred to as the BW model), which treats the isotopic composition of precipitation as the sum of temperature driven rainout effects and regional patterns of vapor sourcing and delivery. Temperature effects are represented by model parameters relating the isotopic composition of precipitation to the absolute value of station latitude ($|LAT|$) and altitude (ALT), according to the equation:

$$p_x = a|LAT_x|^2 + b|LAT_x| + cALT_x, \tag{4}$$

where p_x is an initial estimate of $\hat{\delta}_x$, and a, b, and c are empirical parameters. To represent the effects of regional variation in atmospheric circulation patterns on the isotopic composition of precipitation, we spatially interpolate the δD and $\delta^{18}O$ variability that is not accounted for by the temperature effects described in the equation above. Combining this interpolation with equation (4) gives the composite model equation:

$$\hat{\delta}_x = \frac{\sum_{i=1}^{n} (\delta_i - p_i) e^{(-D_{xi}/\beta_2)}}{\sum_{i=1}^{n} e^{(-D_{xi}/\beta_2)}} + p_x, \tag{5}$$

where β_2 is a distance weighting parameter analogous to β_1. In this study, we fit the model parameters simultaneously by nonlinear least squares, rather than using the two step regression technique proposed by *Bowen and Wilkinson* [2002]. This formulation is more mathematically rigorous in that it assigns equal importance to the latitude and altitude relations, it allows β_2 to be fit to the data, and it ensures a zero mean residual. The frechêt kernels are:

$$\frac{\partial \hat{\delta}_x}{\partial a} = -w_x \sum_{i=1}^{n} \left(|LAT_i|^2 e^{-D_{xi}/\beta_2} \right) + |LAT_x|^2, \tag{6}$$

$$\frac{\partial \hat{\delta}_x}{\partial b} = -w_x \sum_{i=1}^{n} \left(|LAT_i| e^{-D_{xi}/\beta_2} \right) + |LAT_x|, \tag{7}$$

$$\frac{\partial \hat{\delta}_x}{\partial c} = -w_x \sum_{i=1}^{n} \left(ALT_i e^{-D_{xi}/\beta_2} \right) + ALT_x, \tag{8}$$

and:

$$\frac{\partial \hat{\delta}_x}{\partial \beta_2} = -w_x \sum_{i=1}^{n} \left[(\delta_i - p_i) D_{xi} e^{-D_{xi}/\beta_2} \right] + \frac{\sum_{i=1}^{n} \left(D_{xi} e^{-D_{xi}/\beta_2} \right)}{\left(\sum_{i=1}^{n} e^{-D_{xi}/\beta_2} \right)^2} \cdot \sum_{i=1}^{n} \left[(\delta_i - p_i) e^{-D_{xi}/\beta_2} \right], \tag{9}$$

where:

$$w_x = \frac{1}{\sum_{i=1}^{n} e^{-D_{xi}/\beta_2}}. \tag{10}$$

These were implemented in a standard gradient method used to correct a starting model until corrections were small. In most cases, the model converged on a stable solution with less than 20 iterations.

3.2. Interpolated Isotopic Composition of Precipitation

[14] Following comparison of interpolation schemes, we used the GNIP data set and the BW model (which proved to provide the best estimates) to generate global δD and $\delta^{18}O$ grids. Continental grid cell elevations were taken from the ETOPO5 global digital elevation model [*U.S. National Geophysical Data Center*, 1998]. Our grid resolution was $5' \times 5'$ for the continents and $20' \times 20'$ over the oceans, which were treated as cells with 0 m elevation. The reduced spatial resolution of our maps over the oceans is justified in that high-frequency variation in the BW model is primarily driven by topography. Map calculations were performed using the best-fit parameters for all stable isotope data.

3.3. Confidence of Predictions

[15] We calculated 95% confidence intervals for the δD and $\delta^{18}O$ predictions generated by the BW method. The $N - 1$ jackknife was used to estimate the variance of each model parameter and the covariance matrix for the parameters [*Wu*, 1986]. To estimate the variance of the BW estimate at any given grid point, we generated a large number of synthetic parameter sets by drawing each parameter independently and randomly from a uniform distribution with limits determined by the empirically determined parameter variance. For each synthetic parameter set we calculated a δD and $\delta^{18}O$ estimate for the grid point and the probability of that set given the joint probability distribution of the parameters. Our 95% confidence intervals are 1.96 × the probability-weighted mean standard deviation of the estimates derived from the synthetic parameter sets. We found that ~5000 parameter sets were required to produce precise confidence interval estimates. This method is computationally intensive, and as a result we present confidence intervals at $20' \times 20'$ spatial resolution for the continents and $1° \times 1°$ for the oceans.

3.4. Deuterium Excess

[16] We estimated deuterium excess (d [*Dansgaard*, 1964]) at $20' \times 20'$ resolution directly from our δD and $\delta^{18}O$ grids according to:

$$d_x = \hat{\delta}D_x - 8\left(\hat{\delta}^{18}O_x\right). \tag{11}$$

Confidence intervals (95%) were calculated from the standard distribution of deuterium excess values, given by the equation:

$$\sigma_{d,x} = \sqrt{\sigma^2_{\hat{\delta}D_x} + 64\left(\sigma^2_{\hat{\delta}^{18}O_x}\right)}, \tag{12}$$

were $\sigma^2_{\hat{\delta}_x D_x}$ and $\sigma^2_{\hat{\delta}_x {}^{18}O_x}$ indicate the variances of the δD and $\delta^{18}O$ estimates, respectively, calculated above.

4. Results and Discussion

4.1. Comparison of Interpolation Schemes

[17] The value chosen for the weighting radius β_1 affects the spatial scale over which data is averaged to derive

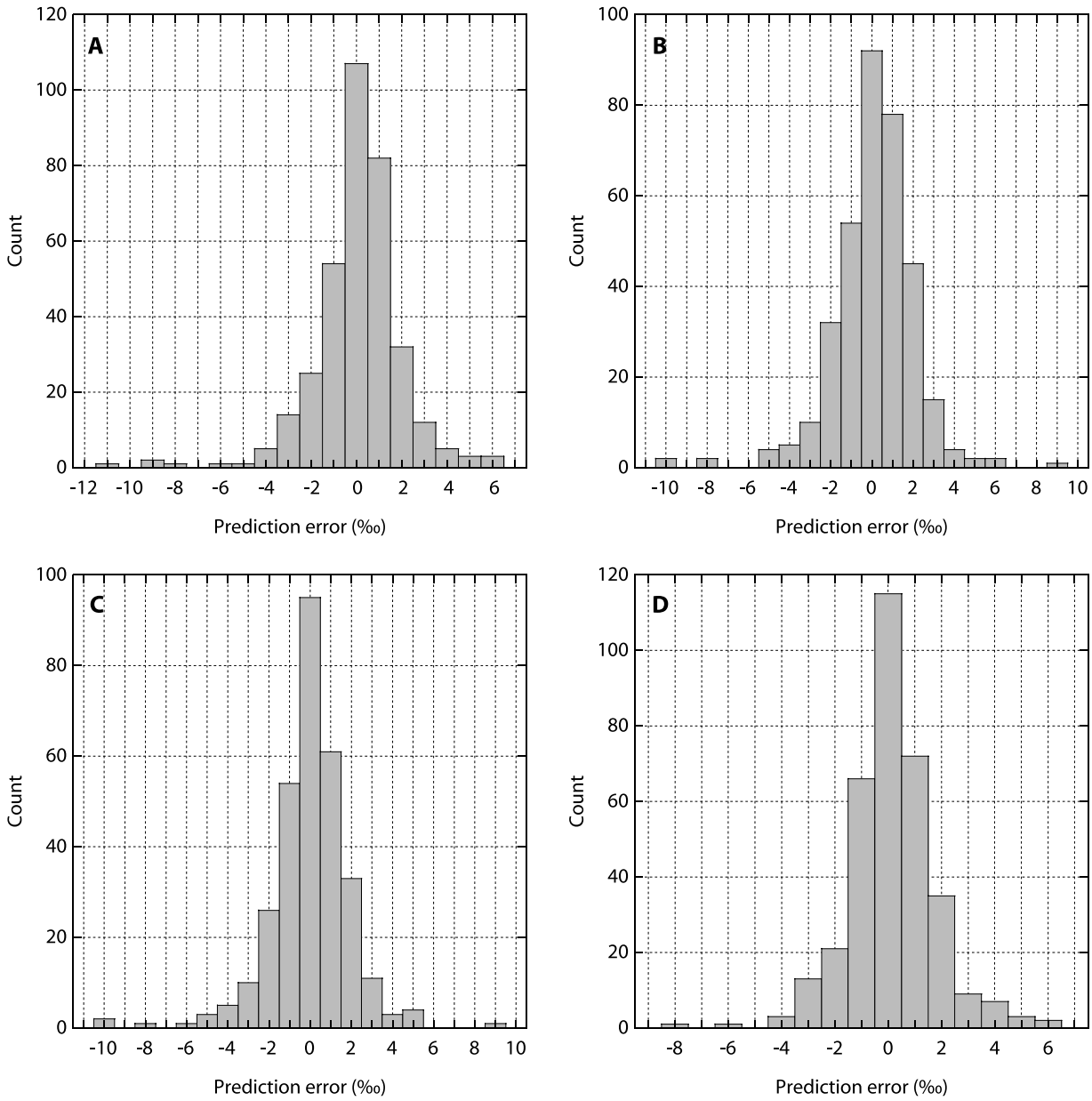

Figure 2. Frequency distributions for the estimation error at the 348 stations in the $N - 1$ $\delta^{18}O$ jackknife for the (a) triangulation, (b) inverse distance, (c) Cressman, and (d) BW methods. Prediction error equals the difference between the $\delta^{18}O$ value measured at a GNIP station and that predicted by interpolation between all other stations. Error distributions are roughly symmetric and strongly peaked (leptokurtic).

interpolations using the inverse distance method. By comparing the quality of predictions made using $\beta_1 = 1$, 2 and 4°, we determine that the optimal weighting radius for this method is ~2°; we therefore use $\beta_1 = 2°$ throughout the rest of this study. The frequency distribution for estimation error for the $N - 1$ $\delta^{18}O$ jackknife under each of the 4 interpolation methods (Figure 2) is roughly symmetric, but leptokurtic (strongly peaked). This distribution is typical of all methods and sample sizes, and we therefore choose to use the L1 norm (average magnitude of error) rather than the L2 norm (mean square error) to highlight differences between interpolation methods. The L1 norm is more sensitive to differences in the body of the probability distributions, and less so to those in the tails, and thus provides an appropriate metric for comparing leptokurtic distributions.

[18] We compare the 4 interpolation methods for δD (Figure 3) and $\delta^{18}O$ (Figure 4) estimates. Comparisons between methods at sites within 10 arc degrees of a data station included in the jackknife subsample (Figures 3a and 4a) allow for the evaluation of the the Cressman method relative to the others, but bias the trend of overall prediction error relative to n because a larger number of stations are excluded from the comparison at low values of n. Patterns of variation in the average magnitude of prediction error are very similar for δD and $\delta^{18}O$. For all interpolation methods, prediction error declines approximately as a negative power

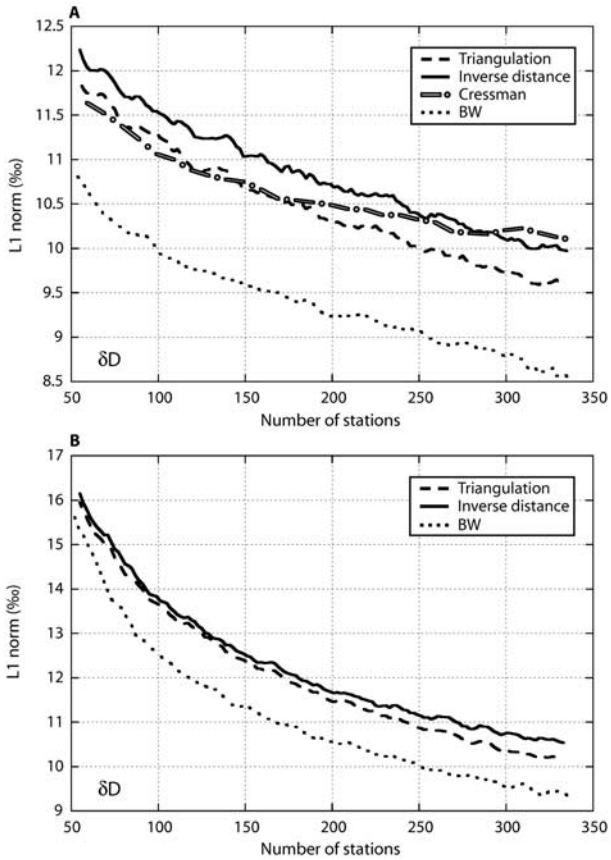

Figure 3. Average magnitude of δD estimation error (L1 norm), plotted against the number of data used in the interpolation. Values in Figure 3a were calculated only for estimation at points within 10 arc degrees of a data station, allowing comparison between all methods. For most sample sizes the BW method has an average magnitude of error ~1.0‰ less than the other methods, with triangulation providing the second best estimates. Values calculated based on estimates at all stations (Figure 3b) show the unbiased trends in estimation error with data number and indicate the average magnitude of error expected for interpolation at a randomly selected location using a given method and number of data. The Cressman method does not produce estimates for sites more than 10 arc degrees from the nearest data station, and cannot be compared to the other methods using this method. Estimation error decreases as more data are used, and does not approach an asymptotic limit at high *n*.

function as the number of included data stations (*n*) increases. At all values of *n*, the BW method provides more accurate estimates relative to the other methods by approximately 1.0‰ for δD and 0.18‰ for $\delta^{18}O$, with triangulation providing the next best estimates for most subsample sizes.

[19] Figures 3b and 4b compare the average prediction error for all interpolation methods except the Cressman method and all sites regardless of their proximity to sampled data stations. As noted above, the relation between average prediction error and the number of data stations is similar for δD and $\delta^{18}O$. For all values of *n*, the average prediction errors for the inverse distance and triangulation methods are similar, with triangulation producing slightly better results. The average prediction error for the BW method is at least 0.7‰ δD and 0.14‰ $\delta^{18}O$ less than that for either triangulation or inverse distance interpolation for all values of *n*. Given the current coverage of the GNIP database, the average magnitude of error associated with point estimates made using the BW method is ~9.4‰ for deuterium and ~1.17‰ for oxygen.

[20] The increase in average estimation error with decreasing data density bears on our ability to reconstruct short-term (interannual) variation in the spatial distribution of stable water isotopes in precipitation. For example, the average δD prediction error for a network of 50 stations is >1.5 times greater than for a network of 340 stations (Figure 3b). In the entire GNIP database, there are only 44 intervals of 12 consecutive months (out of 469 possible) for which δD is known at 50 or more sites, and the greatest number of observations in any such interval is 61. Thus lack of synchronous, short-term data is likely to impose severe limitations on our ability to uncover interannual patterns of variation in the spatial distribution of δD and $\delta^{18}O$ of precipitation.

4.2. Patterns of Error

[21] To further investigate error associated with estimating the stable isotopic composition of precipitation from a

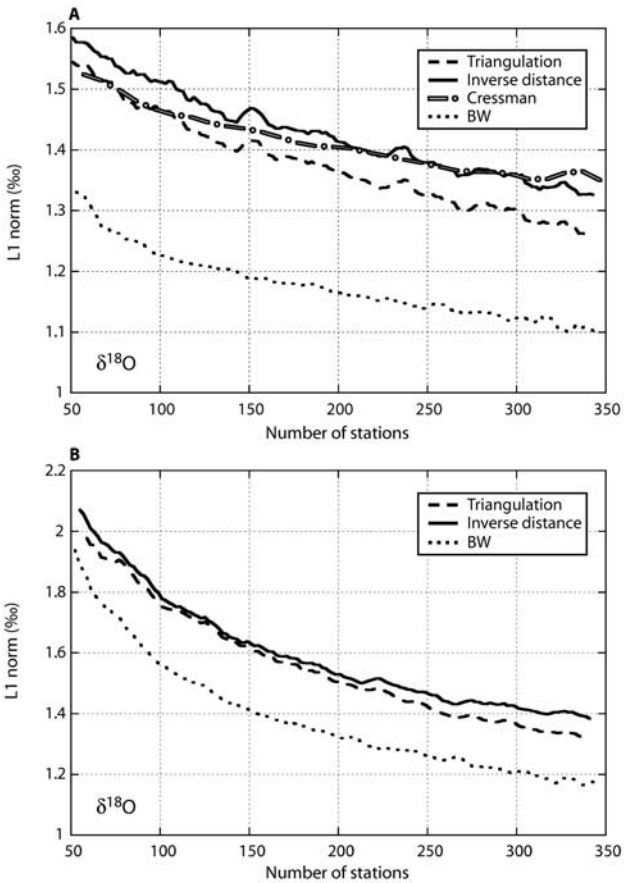

Figure 4. Average magnitude of $\delta^{18}O$ estimation error (L1 norm), plotted against the number of data used in the interpolation. Panels are as in Figure 3. The patterns for $\delta^{18}O$ are similar to those for δD (Figure 3), with the BW method having an average $\delta^{18}O$ estimation error ~0.18‰ less than the other methods at most data densities.

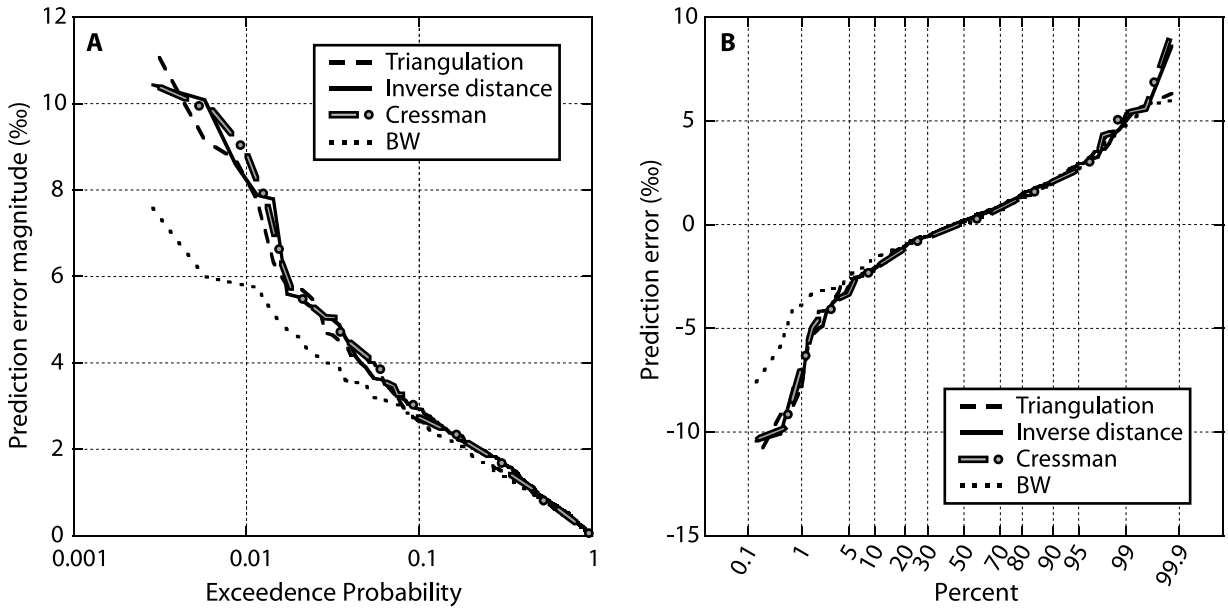

Figure 5. Probability distributions for estimation error in the $N - 1$ $\delta^{18}O$ jackknife. Symbols as in Figure 3. (a) Exceedence probability plot for unsigned error. The BW method provides modest improvement over the other methods in the lower 90% of the error distribution; the most substantial improvement comes in the upper 10%, where estimation error is reduced by up to 3‰. (b) Probability distribution for signed error. The largest differences among methods occur in the tails of the distributions, especially in the lower 5%. The improvement offered by the BW model at these stations, where purely spatial models significantly overestimate the $\delta^{18}O$ of precipitation, may derive in part from the incorporation of altitude effects in the BW model.

large data set by interpolation, we more closely examine the results of the $N - 1$ jackknife analysis for $\delta^{18}O$ (Figure 5). All methods perform similarly over the 90% of their error distributions where $\delta^{18}O$ is estimated most accurately, and for these stations the magnitude of estimation error is less than ~2.5‰ (Figure 5a). Within the remaining 10% of the distribution, however, the BW method reduces the magnitude of error by up to 3‰ relative to the others. Comparing the probability distribution for signed error among methods (Figure 5b), we see that a large part of this improvement is due to the reduction of error at stations where the models produce large, negative errors (i.e., model predicted values are much greater than the measured values). One possible explanation for this pattern is that the inclusion of elevation as a variable in the BW model improves the quality of predictions for high-altitude sites where models that ignore topography would tend to overestimate $\delta^{18}O$. Comparison of the correlation between signed error and station elevation for the 4 methods (Table 1) shows that all methods except the BW method do exhibit a significant relation between these quantities, and supports the hypothesis that some of the improvement offered by the BW scheme is due to incorporation of altitude effects. All methods show a significant relation between magnitude of error and distance between the estimation location and the nearest data station (Table 1). This highlights the fact that all the methods investigated rely, to some degree, on spatial interpolation between proximal data stations to describe regional variations in δD and $\delta^{18}O$.

[22] Lastly, we investigated the relations between the BW model parameters and n, the number of data stations used to fit the model. Significant relations were seen between n and β_2, the distance weighting term, and between n and the root mean square error (RMSE) for the fit between the model and data (Figure 6). Both parameters decrease as n increases. The decrease of β_2 as n increases indicates that as the number and spatial density of data stations increases the model adjusts to describe isotopic variation at smaller spatial scales. Coincident reduction of RMSE for the model fit demonstrates that, through the β_2 adjustment, the model is describing a larger proportion of the variance in the data. The decrease of these parameters with increasing n persists throughout the range of n investigated and does not show strong asymptotic behavior, suggesting that the addition of new data stations should further decrease the spatial scale

Table 1. Correlation Between $\delta^{18}O$ Estimation Error and Physical Variables

Estimation Method	Δ_{error}(‰)/Δ_{alt}(km)[a, b]	Δ_{error}(‰)/$\Delta_{distance}$(°)[a, c]
Triangulation	−1.07 (<0.0001)	0.07 (<0.001)
Inv. dist. (β_1 = 2°)	−1.23 (<0.0001)	0.06 (<0.001)
Cressman[d]	−1.16 (<0.0001)	0.11 (<0.001)
BW	−0.07 (0.63)	0.08 (<0.0001)

[a]The p values for the significance of slopes given in parentheses.
[b]Regression slope between signed error and site altitude; Δ_{alt} is change in altitude.
[c]Regression slope between unsigned error and distance to nearest data station in arc degrees; $\Delta_{distance}$ is change in distance between estimation site and nearest data station.
[d]Regressions for the Cressman method only consider estimation at sites within 10° of a data station.

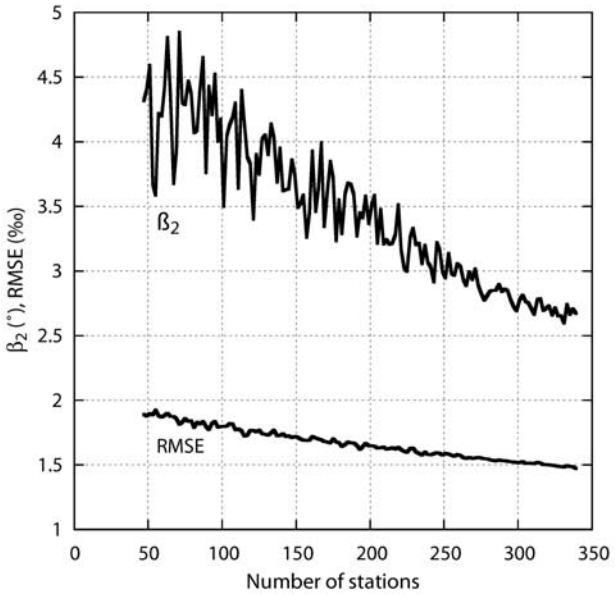

Figure 6. The distance weighting term β_2 and root mean square error (RMSE) for the BW $\delta^{18}O$ model fit at a variety of station densities. Both parameters decrease in an approximately linear fashion as the number of stations increases. The nearly linear decrease of β_2 suggests that at higher spatial station densities, the model is able to describe patterns in the $\delta^{18}O$ fields at a finer spatial resolution. Coincident, linear decrease of the RMSE for the model fit shows that the model describes a greater proportion of the data variance as the number of data increases, and suggests that this trend will continue as more stations are added.

over which δD and $\delta^{18}O$ variation can be described and increase the goodness of fit of the BW model.

4.3. Spatial Distribution of Water Isotopes in Precipitation

[23] Maps representing our optimal (BW model), interpolated δD and $\delta^{18}O$ values for modern mean annual precipitation (Figures 7a and 8a) clearly depict patterns that are expected based on observation and theoretical considerations, including: (1) decreasing δD and $\delta^{18}O$ from the lower midlatitudes toward the poles [*Dansgaard*, 1964], (2) a local decrease in the δD and $\delta^{18}O$ of precipitation from the lower midlatitudes to equatorial regions of high precipitation [*Rozanski et al.*, 1993], (3) lower δD and $\delta^{18}O$ values at high elevations [*Dansgaard*, 1964], and (4) depletion of the heavy isotopes from coastal regions toward the continental interiors [*Rozanski et al.*, 1993]. Effects 1 and 3 can be seen globally on both maps. Effect 2 is most apparent over equatorial Southeast Asia and the equatorial Atlantic and Pacific oceans. Effect 4 is most evident across northern Eurasia and North America. With the exception of effect 2, these patterns can be attributed to the preferential condensation of vapor molecules containing heavy isotopes during progressive rainout, commonly modeled as a Raleigh-type process. Effect 2 is thought to result from decreased evaporative enrichment of the heavy isotope in raindrops falling in large-volume precipitation events or through a more humid equatorial atmosphere. Effects 1–3 are directly represented by the empirical part of our interpolation model. Effect 4 is represented through the spatial interpolation; therefore its depiction on our maps depends on the presence of data stations that document regional heavy isotope depletion in the continental interiors.

[24] In addition to these previously documented effects, one of the most dramatic patterns depicted in both maps is the enhanced zonal heterogeneity of the stable isotope composition of precipitation at high northern latitudes. For example, the interpolated δD of precipitation at 60° north latitude ranges from a low of −170‰ over southeastern Alaska, to a high of −50‰ in the central north Atlantic, and the interpolated δD at sea level over the Atlantic ocean at this latitude is 45‰ heavier than that over the Pacific. *Bowen and Wilkinson* [2002] pointed out that this effect is likely due to elevated zonal heterogeneity of vapor transport patterns at high latitudes. In the case of our example, the anomalously high δD and $\delta^{18}O$ values of precipitation falling over the north Atlantic ocean can be attributed to the influence of the Gulf Stream current, which brings relatively warm water to this ocean. The presence of warm water provides a local source for vapor and reduces the latitudinal temperature gradient over this region, resulting in less rainout from northward-moving air masses. Representation of this effect in the modern isotopic fields suggests that substantial deviations from this pattern in isotopic archive records could be related to change in the oceanic and/or atmospheric circulation regimes affecting this region.

4.4. Confidence of Predictions

[25] The 95% confidence intervals for the δD and $\delta^{18}O$ predictions (Figures 7b and 8b) range from 0.5 to 45‰ for δD and from 0.05 to 6.5‰ for $\delta^{18}O$. Confidence intervals are largest at high latitudes and smallest in low- to midlatitude regions with substantial data coverage. This reflects, in part, the poorer fit of the empirical relation between latitude and δD or $\delta^{18}O$ at high latitudes. In general, confidence intervals are reduced in the vicinity of data stations, and even at high latitudes the confidence intervals near data stations are commonly 4‰ or less for δD and 0.5‰ or less for $\delta^{18}O$. Confidence intervals are slightly higher at high altitudes than for adjacent low altitude areas, reflecting a small uncertainty in the isotope/altitude relation.

[26] In some cases, bands or "bull's-eye" regions of large confidence intervals occur in close proximity to data stations, for example in eastern Alaska, over the Himalayas, and in eastern and Saharan Africa. In each of these cases, increased uncertainty of prediction arises from spatial juxtaposition of data that conflict in the spatial interpolation portion of our model. In some cases the conflict may indicate the presence of stations where measured values represent anomalous years, but in others there may be a mechanistic explanation for the conflict. For example, in Alaska and the Himalayas, this effect likely results from the close proximity of coastal stations, with relatively high δD and $\delta^{18}O$ values, and inland stations receiving precipitation relatively depleted in the heavy isotopes. Resulting bands of high confidence intervals reflect uncertainty in the spatial patterns of rainout over these regions. The "bullseye" patterns in Africa occur around high-altitude stations that receive precipitation with anomalously high δD or $\delta^{18}O$ values that are close to the values recorded at nearby low-altitude stations. We previously noted that the slope of the $\delta^{18}O$/altitude relation in eastern Africa is significantly less

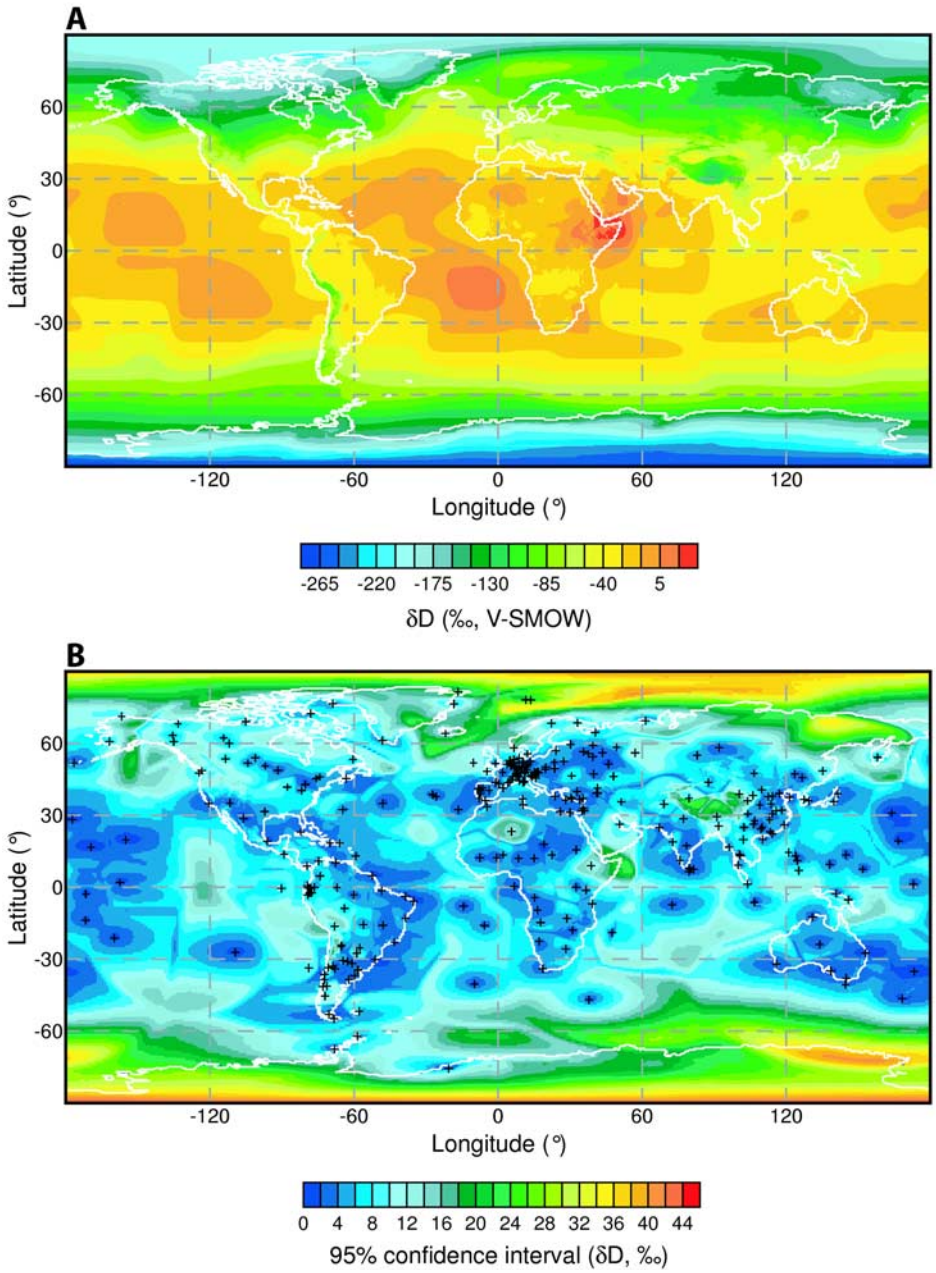

Figure 7. (a) Interpolated δD of precipitation and (b) 95% confidence intervals for these estimates. These maps were made using the BW method, GNIP station data (crosses in Figure 7b), and digital elevation data, as described in the text. See text for discussion.

than the global average [*Bowen and Wilkinson*, 2002]; this contributes to the unusual high-altitude δD or $\delta^{18}O$ values and increased uncertainty of predictions for this region.

[27] Comparison of maps of estimated δD and $\delta^{18}O$ with those of confidence intervals reveals the relative robustness of patterns depicted on the isotope maps and indicates regions where additional water isotopes in precipitation data is most needed. For example, Figures 7a and 8a indicate depletion of the heavy isotopes in rainwater falling over eastern Siberia, but Figures 7b and 8b reveal that the confidence of the estimates in this region is low and suggests that these patterns may be spurious. This region, polar regions, Greenland, much of North America, and areas discussed in the preceding paragraph are areas where high confidence intervals indicate that our understanding of the spatial distribution of stable water isotopes in precipitation would benefit substantially from future monitoring efforts. Integration of stable isotope measurements on snowpack from Antarctica and Greenland might also provide valuable data constraining interpolated δD and $\delta^{18}O$ estimates for these areas.

4.5. Deuterium Excess

[28] Deuterium excess in precipitation is a useful tracer of vapor source and has been related to meteorological conditions at vapor source regions [e.g., *Rozanski et al.*, 1993] and to vapor recycling over the continents [e.g., *Gat et al.*, 1994]. Deuterium excess values calculated from our δD and

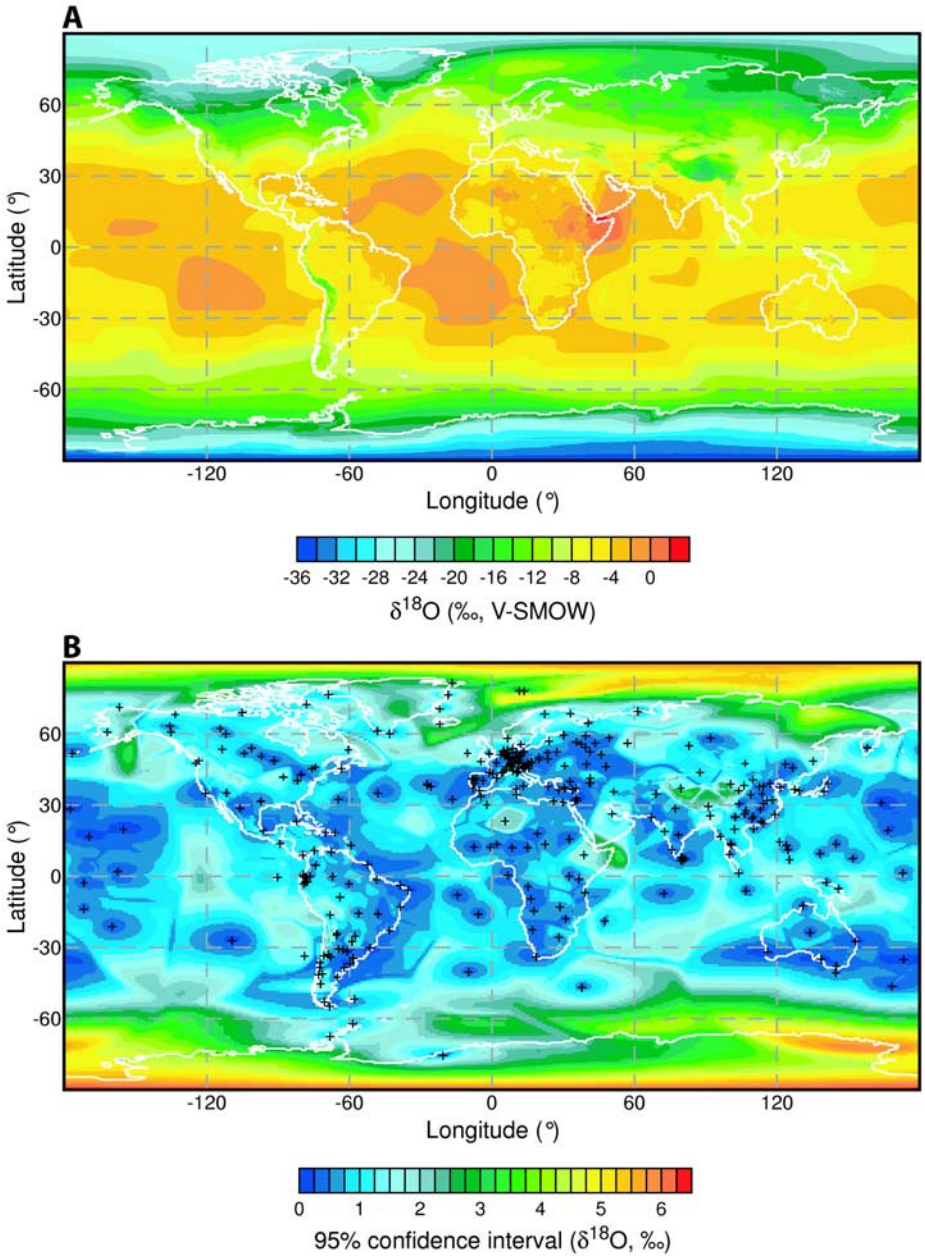

Figure 8. (a) Interpolated $\delta^{18}O$ of precipitation and (b) 95% confidence intervals for these estimates. These maps were made using the BW method, GNIP station data (crosses in Figure 8b), and digital elevation data, as described in the text. See text for discussion.

$\delta^{18}O$ maps show a wide range, with extreme values less than −5‰ and greater than 20‰ (Figure 9a). The global mean value of *d* is approximately 10‰, and using our statistical analysis of the interpolated δD and $\delta^{18}O$ estimates presented above we are able to highlight regions where *d* deviates significantly from this value (Figure 9b). We find that large regions where *d* is significantly different from the global mean are few and, in general, correspond to locations where unusual deuterium excess values have been recognized based on single-station data [*Rozanski et al.*, 1993]. These include areas of high *d* in the eastern Mediterranean, northern Africa, and western Australia and low *d* values over the Antarctic Peninsula, Kamchatka, and southern Greenland. *Merlivat and Jouzel* [1979] have shown that *d* over oceanic vapor source regions is very sensitive to the relative humidity of the atmosphere, with greater relative humidity producing lower *d* values. Comparison of our map with maps of stratospheric humidity [*Peixoto and Oort*, 1996] indicates a close correspondence between the main regions of low *d* and those characterized by high annual average relative humidity (>85%). Furthermore, the significant high-*d* anomalies shown in Figure 9b are uniformly associated with regions of low humidity (<50%) in the lower stratosphere.

[29] It is important to note that Figure 9b indicates only the confidence that estimated *d* values are different from the global mean value, and that other patterns depicted on the map may also be significant. For example, *Gat et al.* [1994]

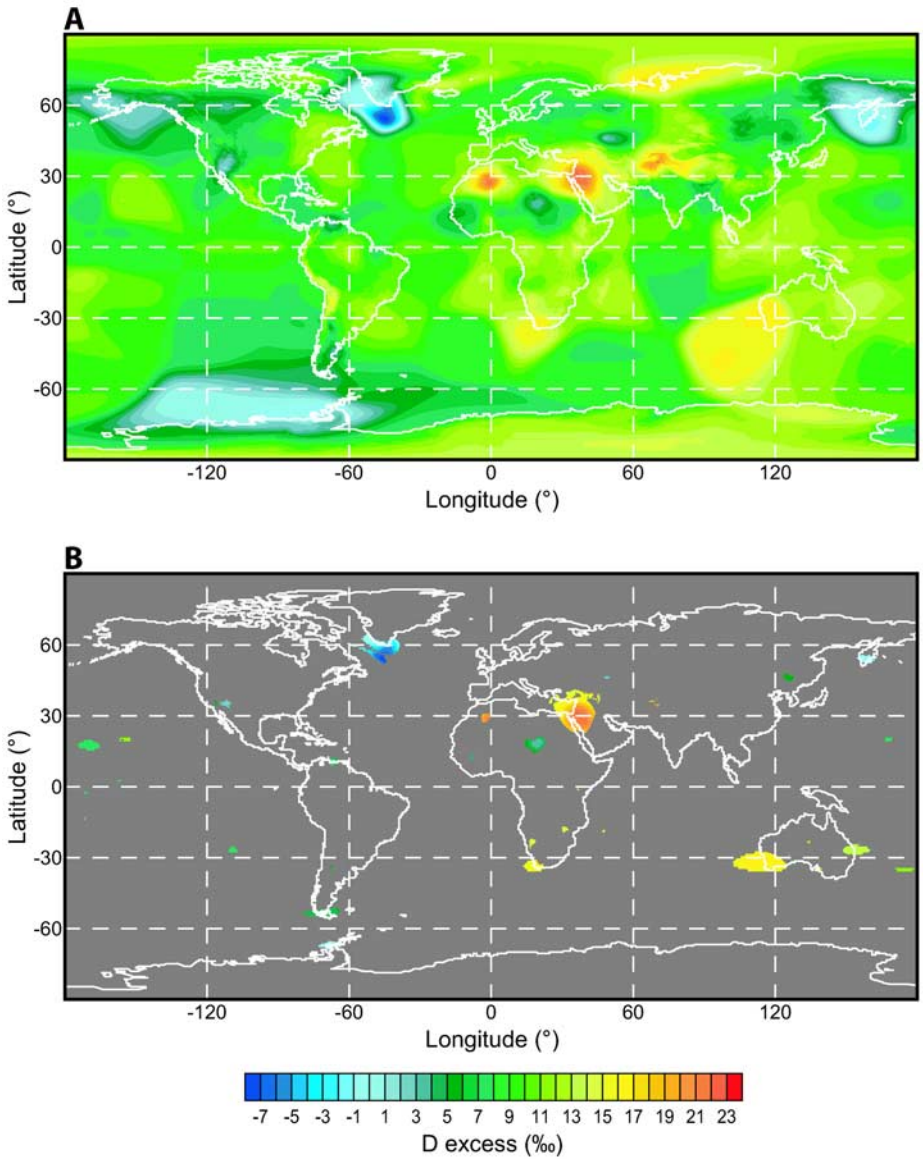

Figure 9. (a) Deuterium excess, calculated from interpolated δD and $\delta^{18}O$ shown in Figures 7 and 8. (b) As in Figure 9a, but regions where the 95% confidence interval for D excess includes the global mean value (10‰) are masked with gray; regions where the D excess is significantly different from the global mean value are unmasked.

examined the *d* of precipitation and river waters over the northern United States and Canada and found that the *d* values of precipitation to the east of the Great Lakes are much greater than those to the west, a phenomenon that they attribute to the contribution of evaporated lake water to atmospheric moisture. This pattern is clearly depicted in the *d* values shown in Figure 9. Patterns of *d* variation are apparent on the global scale, as well, including considerable variation of *d* with latitude (Figure 10a). The high deuterium excess shown for the polar regions in Figure 10a is very poorly constrained and cannot be considered meaningful. The other patterns shown are consistent with the geographic distribution of significant *d* anomalies (Figure 9b) and are likely more robust; these may be related to meteorological conditions over oceanic vapor source regions. In particular, variation of *d* with latitude closely mirrors that of atmospheric relative humidity over the oceans (Figure 10b) [*Peixoto and Oort*, 1996]. Further statistical tests are required to evaluate the significance of regional and global *d* patterns as depicted through interpolated stable isotope fields, but our analysis provides the groundwork for conducting such tests on a case-by-case basis.

5. Conclusions

[30] Comparison of four methods for the spatial interpolation of δD and $\delta^{18}O$ in precipitation data shows that the method proposed by *Bowen and Wilkinson* [2002], and modified here, reduces the average error of estimates by 10–15% relative to other methods tested. The magnitude of

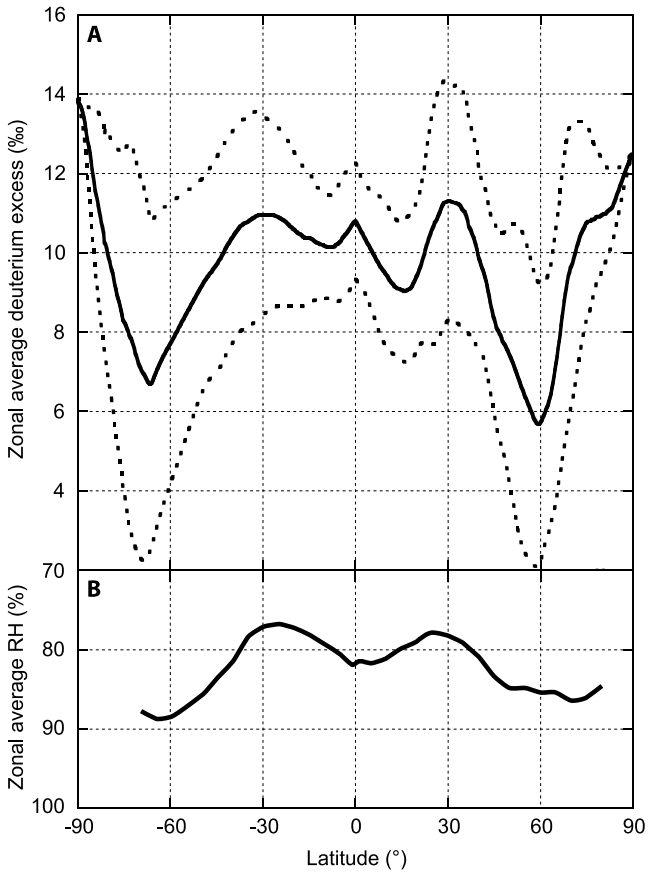

Figure 10. (a) Zonal average deuterium excess (solid line). Dotted lines show ±1 standard deviation from the zonal mean. (b) Schematic representation of the zonal average relative humidity (RH) over oceanic regions, after *Peixoto and Oort* [1996].

error reduction is consistent over a wide range of data densities, although the average magnitude of error for all methods increases substantially as the number of data stations in the training set is reduced. Increased accuracy of the BW method seems to result in part from substantial reduction of high-magnitude errors; this method predicts δD and $\delta^{18}O$ better at the stations where all methods perform most poorly. The other three methods (triangulation, inverse distance weighted interpolation, and Cressman objective analysis) each perform equally well over the range of data densities examined, although triangulation may provide modest improvements relative to the other methods when a large number of data is available. Given the current data density of 340 stations for δD and 348 stations for $\delta^{18}O$, the average magnitude of prediction error for the BW method is 9.4 and 1.17‰ for δD and $\delta^{18}O$, respectively.

[31] Using the BW method, we generate high-resolution global maps of the estimated δD and $\delta^{18}O$ of precipitation with continental and oceanic coverage. Spatial patterns depicted in these maps reflect effects predicted based on theory or previously observed by measurement, including meridional, altitudinal, and continental rainout effects and the tropical "amount effect" [*Rozanski et al.*, 1993]. In addition, the maps depict regional patterns in the spatial distribution of stable water isotopes in precipitation related to meteorological and climatological phenomena such as a plume of heavy water precipitating over the north Atlantic. Maps of the estimated 95% confidence intervals for the interpolated δD and $\delta^{18}O$ of precipitation give a quantitative measure of the robustness of spatial patterns depicted on the δD and $\delta^{18}O$ maps, highlight regions where some data are unusual when viewed in a regional context, and indicate areas where additional data are most needed. The isotope and confidence interval maps can be interpreted in conjunction to investigate complex spatial patterns in the δD and $\delta^{18}O$ data sets; we provide an example where we map regions of extreme deuterium excess values. These maps present a quantitative, statistically robust depiction of the spatial distribution of stable water isotopes in precipitation, and can be used to provide input functions for stable isotope hydrology models, as a benchmark against which output from isotope tracer-equipped GCMs can be compared, and as a template for the interpretation of δD and $\delta^{18}O$ archive records.

[32] **Acknowledgments.** This manuscript was improved by discussions with and reviews by S. J. Birks, P. L. Koch, B. H. Wilkinson, and two anonymous reviewers. We acknowledge the considerable effort of scientists associated with the GNIP program in the collection and compilation of the data that made this analysis possible. Partial support was provided by National Science Foundation (NSF) grant ATM-0222383 and Biocomplexity grant EAR-0120727. G.J.B. is supported by the NSF Graduate Research Fellowship Program.

References

Amundson, R. G., O. A. Chadwick, C. Kendall, Y. Wang, and M. J. DeNiro, Isotopic evidence for shifts in atmospheric circulation patterns during the late Quaternary in mid-North America, *Geology*, *24*, 23–26, 1996.

Birks, S. J., J. J. Gibson, L. Gourcy, P. K. Aggarwal, and T. W. D. Edwards, Maps and animations offer new opportunities for studying the global water cycle, *Eos Trans. AGU Electron. Suppl.*, *83*(37), 10 Sept. 2002. (Available at http://www.agu.org/eos_elec/020082e.html)

Bowen, G. J., and B. Wilkinson, Spatial distribution of $\delta^{18}O$ in meteoric precipitation, *Geology*, *30*, 315–318, 2002.

Boyle, E. A., Cool tropical temperatures shift the global $\delta^{18}O$-T relationship: An explanation for the ice core $\delta^{18}O$-borehole thermometry conflict?, *Geophys. Res. Lett.*, *24*, 273–276, 1997.

Chamberlain, C. P., and M. A. Poage, Reconstructing the paleotopography of mountain belts from the isotopic composition of authigenic minerals, *Geology*, *28*, 115–118, 2000.

Chamberlain, C. P., M. A. Poage, D. Craw, and R. C. Reynolds, Topographic development of the Southern Alps recorded by the isotopic composition of authigenic clay minerals, South Island, New Zealand, *Chem. Geol.*, *155*, 279–294, 1999.

Cressman, G. P., An operative objective analysis system, *Mon. Weather Rev.*, *87*, 367–374, 1959.

Dansgaard, W., Stable isotopes in precipitation, *Tellus*, *16*, 436–468, 1964.

Dansgaard, W., et al., Evidence for general instability of past climate from a 250-kyr ice-core record, *Nature*, *364*, 218–220, 1993.

Edwards, T. W. D., B. B. Wolfe, and G. M. MacDonald, Influence of changing atmospheric circulation on precipitation $\delta^{18}O$-temperature relations in Canada during the Holocene, *Quat. Res.*, *46*, 211–218, 1996.

Emiliani, C., Quaternary paleotemperatures and the duration of the high-temperature intervals, *Science*, *178*, 398–401, 1972.

Gat, J. R., C. J. Bowser, and C. Kendall, The contribution of evaporation from the Great Lakes to the continental atmosphere: Estimate based on stable isotope data, *Geophys. Res. Lett.*, *21*, 557–560, 1994.

Genty, D., V. Plagnes, C. Causse, O. Cattani, M. Stievenard, S. Falourd, D. Blamart, R. Ouahdi, and S. Van-Exter, Fossil water in large stalagmite voids as a tool for paleoprecipitation stable isotope composition reconstitution and paleotemperature calculation, *Chem. Geol.*, *184*, 83–95, 2002.

Hammarlund, D., L. Barnekow, H. J. B. Birks, B. Buchardt, and T. W. D. Edwards, Holocene changes in atmospheric circulation recorded in the oxygen-isotope stratigraphy of lacustrine carbonates from northern Sweden, *Holocene*, *12*, 339–351, 2002.

Hays, P. D., and E. L. Grossman, Oxygen isotopes in meteoric calcite cements as indicators of continental paleoclimate, *Geology*, *19*, 441–444, 1991.

Hobson, K. A., and L. I. Wassenaar, Linking breeding and wintering grounds of neotropical migrant songbirds using stable hydrogen isotopic analysis of feathers, *Oecologia*, *109*, 142–148, 1997.

Jahren, A. H., and L. S. L. Sternberg, Eocene meridional weather patterns reflected in the oxygen isotopes of Arctic fossil wood, *GSA Today*, *12*, 4–9, 2002.

Jouzel, J., G. Hoffmann, R. D. Koster, and V. Masson, Water isotopes in precipitation: Data/model comparison for present-day and past climates, *Quat. Sci. Rev.*, *19*, 363–379, 2000.

Kendall, C., and T. B. Coplen, Distribution of oxygen-18 and deuterium in river waters across the United States, *Hydrol. Processes*, *15*, 1363–1393, 2001.

Lauritzen, S.-E., Calibration of speleothem stable isotopes against historical records; a Holocene temperature curve for north Norway?, in *Climate Change*: *The Karst Record*, *Karst Waters Inst. Spec. Publ.*, vol. 2, edited by S.-E. Lauritzen, pp. 78–80, Karst Waters Inst., Gainesville, Florida, 1996.

Lee, K. S., D. B. Wenner, and I. Lee, Using H- and O-isotopic data for estimating the relative contributions of rainy and dry season precipitation to groundwater: Example from Cheju Island, Korea, *J. Hydrol.*, *222*, 65–74, 1999.

Mathieu, R., D. Pollard, J. E. Cole, J. W. C. White, R. S. Webb, and S. L. Thompson, Simulation of stable water isotope variations by the GENESIS GCM for modern conditions, *J. Geophys. Res.*, *107*, 4037, 2002.

Merlivat, L., and J. Jouzel, Global climatic interpretation of the deuterium-oxygen 18 relationship for precipitation, *J. Geophys. Res.*, *84*, 5029–5033, 1979.

Peixoto, J. P., and A. H. Oort, The climatology of relative humidity in the atmosphere, *J. Clim.*, *9*, 3443–3463, 1996.

Pierrehumbert, R. T., Huascaran $\delta^{18}O$ as an indicator of tropical climate during the Last Glacial Maximum, *Geophys. Res. Lett.*, *26*, 1345–1348, 1999.

Poage, M. A., D. J. Syostrom, J. Goldberg, C. P. Chamberlain, and G. Furniss, Isotopic evidence for Holocene climate change in the northern Rockies from a goethite-rich ferricrete chronosequence, *Chem. Geol.*, *166*, 327–340, 2000.

Rozanski, K., L. Araguas-Araguas, and R. Gonfiantini, Isotopic patterns in modern global precipitation, in *Climate Change in Continental Isotopic Records*, *Geophys. Monogr. Ser.*, vol. 78, edited by P. K. Swart et al., pp. 1–36, AGU, Washington, D. C., 1993.

Seltzer, G., D. Rodbell, and S. Burns, Isotopic evidence for late Quaternary climatic change in tropical South America, *Geology*, *28*, 35–38, 2000.

Sharp, Z. D., and T. E. Cerling, Fossil isotope records of seasonal climate and ecology: Straight from the horse's mouth, *Geology*, *26*, 219–222, 1998.

Tichelaar, B. W., and L. J. Ruff, How good are our best models? Jackknifing, bootstrapping, and earthquake depth, *Eos Trans. AGU*, *70*(20), 593, 606, 1989.

U.S. Geological Survey, GTOPO30 global 30 arc second elevation data, EROS Data Cent., Sioux Falls, S. D., 1996.

U.S. National Geophysical Data Center, ETOPO-5 five minute gridded world elevation, Boulder, Colo., 1998.

Welker, J. M., Isotopic ($\delta^{18}O$) characteristics of weekly precipitation collected across the USA: An initial analysis with application to water source studies, *Hydrol. Processes*, *14*, 1449–1464, 2000.

Wolfe, B. B., R. Aravena, M. B. Abbott, G. O. Seltzer, and J. J. Gibson, Reconstruction of paleohydrology and paleohumidity from oxygen isotope records in the Bolivian Andes, *Palaeogeogr. Palaeoclimatol. Palaeoecol.*, *176*, 177–192, 2001.

Wu, C. F. J., Jackknife, bootstrap and other resampling methods in regression analysis, *Ann. Stat.*, *14*, 1261–1295, 1986.

G. J. Bowen, Earth Science Department, University of California, 1052 High Street, Santa Cruz, CA 95064, USA. (gbowen@es.ucsc.edu)

J. Revenaugh, Department of Geology and Geophysics, University of Minnesota, 310 Pillsbury Drive SE, Minneapolis, MN 55455, USA.